ADVANCED ENERGY MATERIALS
www.advenergymat.de

Fabrication Strategy for Efficient 2D/3D Perovskite Solar Cells Enabled by Diffusion Passivation and Strain Compensation

*Cuiling Zhang, Shaohang Wu, Leiming Tao, Gowri Manohari Arumugam, Chong Liu, Zhen Wang, Shusheng Zhu, Yuzhao Yang, Jie Lin, Xingyuan Liu, Ruud E. I. Schropp, and Yaohua Mai**

Lattice matching and passivation are generally seen as the main beneficial effects in 2D/3D perovskite heterostructured solar cells, but the understanding of the mechanisms involved is still incomplete. In this work, it is shown that 2D/3D heterostructure are unstable under common thermal processing conditions, caused by the lattice expansion of strained 2D perovskite. Therefore an innovative fabrication technology involving a compressively strained PEA_2PbI_4 layer is proposed to compensate the internal tensile strain and stabilize the 2D/3D heterostructure. Moreover, a small amount of PEA^+ diffusing into the grain boundaries of 3D perovskite forms 2D perovskite and passivates the defects there. Combining the effects of strain compensation and diffusion passivation, the stabilized 2D/3D perovskite solar cells deliver a reproducible and robust laboratory power conversion efficiency (PCE) of 21.31% for the p-i-n type devices, along with a high V_{OC} of 1.18 V. A certified PCE of 20.22% is confirmed by an independent national metrology institute.

The power conversion efficiency (PCE) of single-junction perovskite solar cells (PSCs) has continually risen over the last decade, from 3.8% in 2009 to 25.2% in 2020, rivaling commercial photovoltaic technology, such as Si wafer technology and thin-film technologies like cadmium telluride (CdTe).[1–3] There is a deficit in open-circuit voltage (V_{OC}) for most photovoltaic technologies, that is, a substantial discrepancy between the obtained V_{OC} and the band gap of the absorbing layer. This is thought to be one of the biggest challenges in approaching the maximum theoretical PCE.[4–8] The V_{OC} deficit is usually caused by non-radiative recombination which closely correlates with the defect density in the absorbing layer of PSCs.[9,10]

In PSC technology, component engineering is one of the effective means to reduce the density of trap states. Cs/FA ($CH(NH_2)^{2+}$)/MA ($CH_3NH_3^+$) triple cation perovskites have demonstrated lower trap state density than $MAPbI_3$, resulting in a reduced V_{OC} deficit.[11] Nevertheless, there is still room for further decreasing the V_{OC} deficit, because the defect density of the absorbing layer is still substantial. Furthermore, the interface defect density in PSCs is generally higher than the bulk defect density, as experiments have shown.[12]

Utilizing passivated contacts is an effective method to reduce the interface defects, and low-dimensional perovskite materials, such as PEA_2PbI_4 (PEA: phenethylammonium) and BA_2PbI_4 (BA: butylammonium), have been applied to achieve significant surface passivation. Wang et al. have built-in layered BA_2PbI_4 perovskite at the grain boundaries in 3D perovskite to achieve effective defect passivation.[13] The resulting perovskite films showed a significant decrease in non-radiative recombination owing to the decrease of interface defects. Also PEA_2PbI_4 perovskite has been reported to passivate grain boundaries and reduce the non-radiative recombination lifetime.[14] More recently, You and co-workers proved that perovskites treated by PEAI without further thermal annealing exhibited superb performance, and deduced that PEAI itself has a much better passivation effect than PEA_2PbI_4.[3] However, their results also indicate that PEA_2PbI_4 can be formed at low temperature (<50 °C) from PEAI and PbI_2, therefore the passivation effect caused by PEAI itself will be limited under actual operation.

In addition, residual tensile strain near the interface has been demonstrated to negatively impact both the efficiency and

C. Zhang, Dr. S. Wu, Dr. G. M. Arumugam, C. Liu, Dr. Z. Wang, Dr. Y. Yang, Prof. R. E. I. Schropp, Prof. Y. Mai
Institute of New Energy Technology
College of Information Science and Technology
Jinan University
Guangzhou 510632, China
E-mail: yaohuamai@jnu.edu.cn

Prof. L. Tao
College of Science
Guangdong University of Petrochemical Technology
Maoming 525000, China

S. Zhu
College of Applied Physics and Materials
Wuyi University
Jiangmen 529000, China

Prof. J. Lin, Prof. X. Liu
State Key Laboratory of Luminescence and Applications
Changchun Institute of Optics
Fine Mechanics and Physics
Chinese Academy of Sciences
Changchun 130033, China

The ORCID identification number(s) for the author(s) of this article can be found under https://doi.org/10.1002/aenm.202002004.

DOI: 10.1002/aenm.202002004

stability.[15,16] In general, residual stress is related to the mismatch of lattice constants and/or thermal expansion coefficients between perovskite and interface layers.[17,18] Therefore, lattice matching is considered to be one of the primary advantages of 2D/3D perovskites heterostructures.[19,20] The unit cell parameters of PEA_2PbI_4 ($a = b = 8.74$ Å, $c = 33.00$ Å) have a better structure match with $MAPbI_3$ ($a = b = 8.87$ Å, $c = 12.52$ Å)[21] than the commonly used charge transport materials, such as SnO_2 ($a = b = 4.73$ Å, $c = 3.18$ Å)[22] and TiO_2 ($a = 18.92$ Å, $b = 30.72$ Å).[23] However, the understanding of residual strain and their effects on 2D/3D perovskites heterostructure is still limited.

In this work, we stabilize the 2D/3D perovskites heterostructure via compensating strain by PCBM layer. In addition, high-resolution transmission electron microscopy (HRTEM) reveals that the diffusion of small ions caused by thermal annealing forms 2D passivating structures along grain boundaries, thus reduces the recombination velocity. Due to the combinative effect of diffusion passivation and stress compensation, we have boosted the V_{OC} to 1.18 V, which, along with the short-circuit current density (J_{SC}) of 22.76 mA cm^{-2} and fill factor (FF) of 79.3%, resulted in a PCE of 21.31% measured in our laboratory, and an independently certified PCE of 20.22%.

The commonly used procedure in fabricating 2D/3D perovskites heterostructures is to perform a short-time thermal treatment after covering the 3D perovskite with organic molecules.[24,25] In the present work, we attempted to prolong the annealing time so as to investigate the evolution of 2D/3D perovskites heterostructure. The device structure we adopted is illustrated in Figure S1, Supporting Information, consisting of indium tin oxide (ITO)/polytriarylamines (PTAA)/perovskite (2D and 3D)/[6,6]-phenyl-C61-butyric acid methyl ester (PCBM)/ZnO/Ag. The 3D perovskite films were treated with an optimal PEAI concentration of 1 mg mL^{-1} (Figure S2, Supporting Information). We tested the device performance for different processing times of the PEAI layer varying from 10 min to 4 h and found that the V_{OC} of the device reached a maximum at 2 h and then began to decline (Figure S3 and Table S1, Supporting Information).

To explore the origin of the initial improvement in V_{OC}, X-ray diffraction (XRD) analysis was performed to investigate the crystal structure evolution with increasing annealing time in 2D/3D perovskite film, and the results are displayed in **Figure 1**a. The main peaks of PEA_2PbI_4 and 3D perovskite are magnified to clearly distinguish the changes in specific characteristic peaks. Among all 2D perovskite crystal planes, we chose the (002) diffraction peak for further research owing to its strong diffraction intensity. Because all diffraction peaks of 2D perovskite weaken with increasing annealing time, the data have been normalized to accurately show the shift of peak position. As thermal annealing time increases, the (002) diffraction peak gradually shifts toward lower angles, from 5.40° to 5.34°, hence d_{002} increases from 16.35 to 16.54 Å as derived from the Bragg diffraction equation, $2d \sin\theta = n\lambda$. The characteristic peaks of 3D perovskites remain almost unchanged as expected. The left shift of the characteristic peaks for 2D perovskite may be ascribed to lattice expansion and/or strain evolution.[26] Such thermal-, light-, and bias-induced structural variations have been reported in perovskite films.[27,28]

In order to explore whether the left shift of the characteristic peaks is caused by residual strain, grazing incident X-ray diffraction (GIXRD) was performed. A schematic diagram for the analysis of the residual strain is depicted in Figure S4, Supporting Information. The principle and specific calculation of residual strain can be found in the paper reported by Chen et. al.[29] The GIXRD patterns at different tilt angle for our samples prepared using different annealing times (10 min and 2 h) are shown in Figure 1b,c. In general, $\sin^2\psi$ and 2θ follow a linear relationship, so we can calculate the film stress σ by fitting the 2θ as a function of $\sin^2\psi$ according to the following equation[29]

$$\sigma = -\frac{E}{2(1+\nu)}\frac{\pi}{180}\cot\theta_0\frac{\partial(2\theta)}{\partial\sin^2\psi} \quad (1)$$

where E and ν are Young's modulus and Poisson's ratio, respectively, for the PEA_2PbI_4 thin film. θ_0 is the diffraction peak for a strain-free perovskite crystal plane (here we took the crystal data from the literature)[30] and θ is the diffraction peak for the measured perovskite thin films. ψ is the angle of diffraction vector with respect to the sample normal direction. As shown in Figure 1d, the two fitting lines exhibit almost the same slope, which means that the 2D perovskite annealed for various duration are subjected to similar tensile strain. It is surprising that the tensile stress values of 2D perovskite are actually larger than 1000 MPa. They amount to 1329 and 1348 MPa for PEAI-10 min and PEAI-2 h samples, respectively. The residual strain in the perovskite films was insensitive to the duration of the post-annealing treatment due to the strong adhesion between the perovskite and the contact layer once the perovskite was formed, in line with a previous report.[31] Thus, at this stage we can tentatively conclude that the left shift of the feature peaks originate from lattice expansion.

For PEA_2PbI_4 perovskite crystal, first-principles density functional theory (DFT) calculations have also been carried out to confirm how the crystal changes depend on lattice expansion. The emerging characteristic peak of (002) crystal plane for the PEAI-10 min sample shows good agreement with the simulation results of perfect PEA_2PbI_4 (Figure S5, Supporting Information). In addition, the crystals were fixed in a axis and b axis directions, and stretched along the c axis (Figure S6, Supporting Information). As the stretching extends, the diffraction peak of (002) plane shifts toward lower angles, and d_{002} increases (Tables S2 and S3, Supporting Information), which is in good agreement with our experimental results. This confirms our hypothesis of lattice expansion occurring during the annealing process.

Regarding the mechanism for the lattice expansion, the following possibilities are proposed (Figure 1e). There is very high probability for ionic migration of MA^+ and I^- ions in hybrid perovskite films.[32] Moreover, MA^+ ions tend to enrich the upper half of the 3D bulk, as reported earlier.[29] The 2D perovskite crystals are generally formed by many repeating units, linked by weak Van der Waals interactions.[17] Furthermore, the as-prepared films exhibit a relatively large interstice between long chain molecules because of the steric hindrance.[33] For all the above reasons, MA^+ and I^- ions can easily pass through the

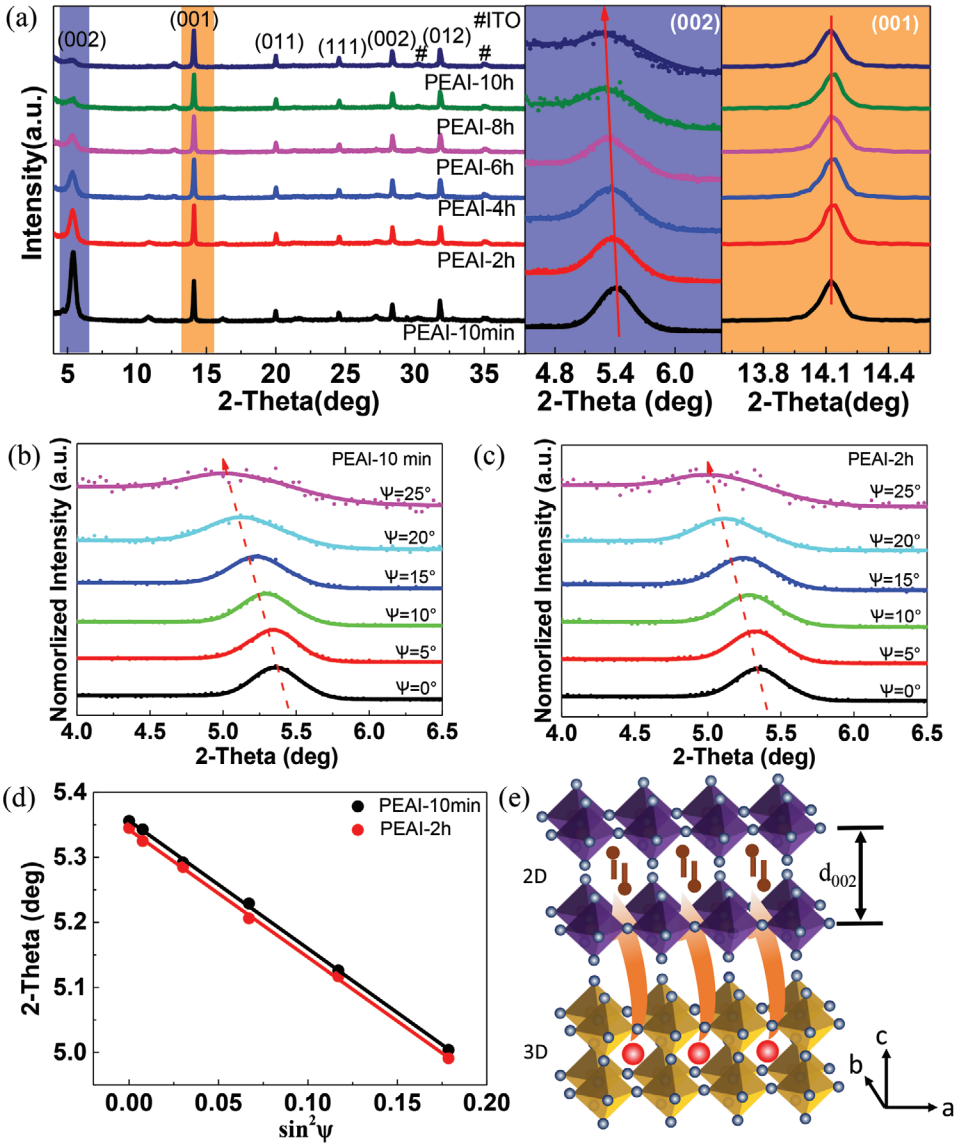

Figure 1. a) XRD patterns for 2D/3D perovskite film as a function of thermal annealing time; magnified and normalized diffraction peaks of (002) plane from 2D perovskite; magnified diffraction peaks of (001) plane from 3D perovskite. GIXRD spectrum at different tilt angles for b) PEAI-10 min and c) PEAI-2 h thin films. d) Residual tensile stresses of PEA_2PbI_4 annealed under different times. e) Schematic diagram of lattice expansion.

$[PbI_6]^{4-}$ octahedral layer and gather in the 2D perovskites under thermal annealing, due to the tightly coupled heterostructure. We speculate that the MA^+ and I^- ions entering the 2D perovskite destroy the weak interaction of its interlayers. Thus, lattice expansion is likely to occur, owing to the elimination of interaction, giving rise to an increase in d_{002}. To substantiate this explanation we shown in Figure S7, Supporting Information, that the diffraction peaks of pure PEA_2PbI_4 perovskite grown on ITO stay at their original position upon thermal annealing.

It is known that 2D perovskites with large interlayer distance generally show quantum confinement of charge carriers.[34,35] Unfortunately, our results show that the interlayer distance increases with the thermal annealing, thus the charge transfer is bound to be limited. Thus, the understanding for device performance improvement upon extended thermal annealing is not complete yet. To explore this further, HRTEM of a cross-section for 2D/3D perovskites heterostructure was used to reveal the microscopic changes at the interface. Figure S8, Supporting Information shows the overview HRTEM image of PEAI-2 h sample cross-section. The perovskite was deposited on ITO and the sample for cross-section imaging was prepared by focused ion beam (FIB) cutting with a protective layer of platinum predeposited on top. **Figure 2**a shows the magnified HRTEM image, which exhibits a well-defined interface that clearly demarcates the PCBM from the 2D perovskite beneath. To provide a detailed insight into the micro-structure of the 2D/3D perovskites heterostructure, a magnified image is acquired at the rectangular area in Figure 2a. As shown in Figure 2b, the layered 2D perovskite shows a starkly different interplanar spacing, as compared to the 3D bulk. At the upper

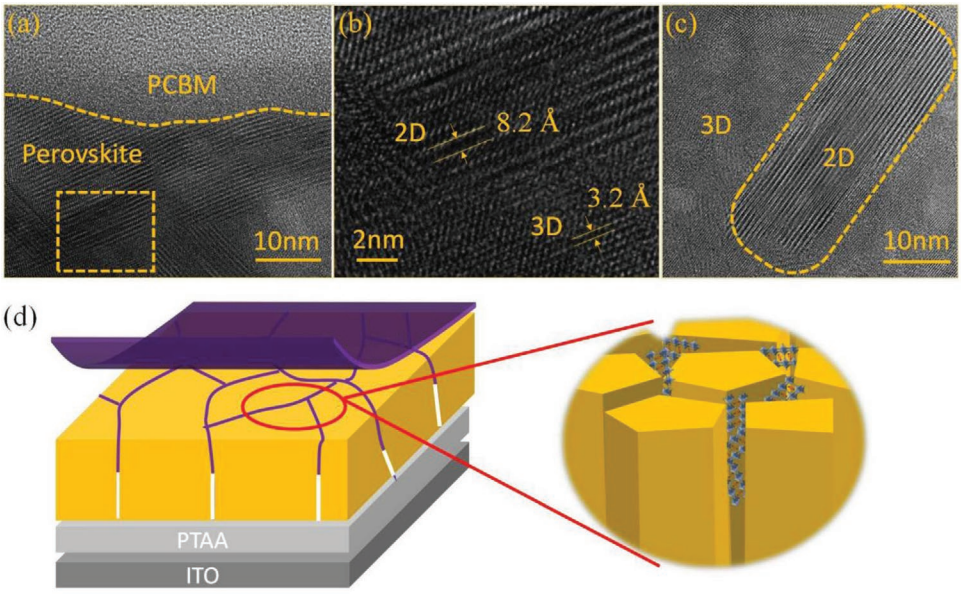

Figure 2. a) HRTEM images for junction of PCBM and perovskite in PEAI-2 h sample. b) Magnified HRTEM image taken from rectangular area of (a). c) HRTEM image on middle part of PEAI-2 h perovskite film. d) The diffusion diagram of 2D perovskite along grain boundaries.

area, the interplanar distance is ≈8.2 Å, corresponding to the layered PEA_2PbI_4 perovskite. The interplanar distance of 3.2 Å at the bottom of the image correlates with the (002) reflection of 3D perovskite. In addition, we found lattice fringes of 2D perovskite when probing deeper from the top along the cross-section of the PEAI-2 h sample (Figure 2c), whereas in PEAI-10 min sample (Figure S8, Supporting Information) they could only be observed near the surface. This confirms our hypothesis that 2D perovskite diffuses progressively downward with longer annealing times.

Some of PEA_2PbI_4 tend to aggregate at the concave grain boundaries of the 3D perovskite. Ion migration through grain boundaries of polycrystalline perovskites is regarded as the dominant mechanism.[36] The calculated results show that Pb^{2+} has higher activation energy for ionic migration than A- and X-site ions.[37] With continued annealing of the perovskite film, PEA^+ ions migrate along the grain boundaries and recrystallize with unreacted PbI_2. This is resembles the recrystallization accompanied with enlarged grain size as is commonly seen in 3D perovskites.[38,39] The result we obtained here is the diffusion of 2D perovskite into the 3D film as a consequence of migration of PEA^+ ions as shown in Figure 2d.

We attribute the changes in V_{OC} after thermal annealing to a trade-off between lattice expansion and thermal diffusion of PEA_2PbI_4. It has been reported that 3D perovskite crystals are unstable under heating, thereby the formation energy of defects and activation energy for ion migration are lowered.[31] Importantly, diffused PEA_2PbI_4 may passivate the defects formed by thermal annealing in 3D perovskite. However, considering the negative effect of lattice expansion caused by thermal annealing, there must be an optimal annealing time for solar cell performance. Therefore, the device annealed for 2 h shows the champion efficiency.

Taking into count the large tensile strain in 2D perovskite, we introduce a strain-compensation strategy to reduce lattice expansion by adding an external compressive strain layer. We optimized our previous preparation process for 2D perovskite and the corresponding procedure chart is displayed in **Figure 3**a. Here, 3D perovskite films were fabricated by one-step spin coating as usual; then PEAI dissolved in isopropanol was deposited on top of 3D perovskite; and finally, the annealing process (time is 2 h) is done after covering the structure with PCBM. The thin film or device fabricated by this means is named PCBM-2 h.

To investigate the impact of upper PCBM on the strain of PEA_2PbI_4, residual strain measurements were conducted again and the results are shown in Figure 3b,c. As expected, the tensile strain for the PCBM-2 h sample is reduced to 983 MPa. The difference in thermal expansion coefficients between perovskite and its contact layers provides an origin of strain.[27] Here, the mismatch of thermal expansion coefficients between the two layers is utilized to realize the purpose of strain compensation. The linear thermal expansion coefficients of PEA_2PbI_4 are $a = 4.857 \times 10^{-5}$ K^{-1}, $b = 8.651 \times 10^{-5}$ K^{-1}, $c = 19.11 \times 10^{-5}$ K^{-1},[40] and the average thermal expansion coefficient of PCBM is 6.2×10^{-5} K^{-1}.[41] The thermal expansion coefficient of PEA_2PbI_4 is universally greater than that of PCBM at the junction region. It has been pointed that there is strong PCBM–iodide interaction in perovskite devices, so PEAI will be well anchored by PCBM.[42] As shown in Figure 3d, it is difficult for PEA_2PbI_4 to stretch along the direction parallel to the substrate due to anchored by PCBM with low thermal expansion coefficient, thus its tensile strain is relieved. Meanwhile, $[PbI_6]^{4-}$ octahedra in PEA_2PbI_4 embedded in the sandwich structure (3D perovskite/PEA_2PbI_4/PCBM) can hardly move due to clamping on both sides, which means that MA^+ and I^+ ions are less likely to migrate into 2D perovskite. The peak positions of 2D perovskite films show just a slight shift after 253 h of thermal annealing when the films are covered by PCBM (Figure 3e and Figure S9, Supporting Information). These observations suggest that the

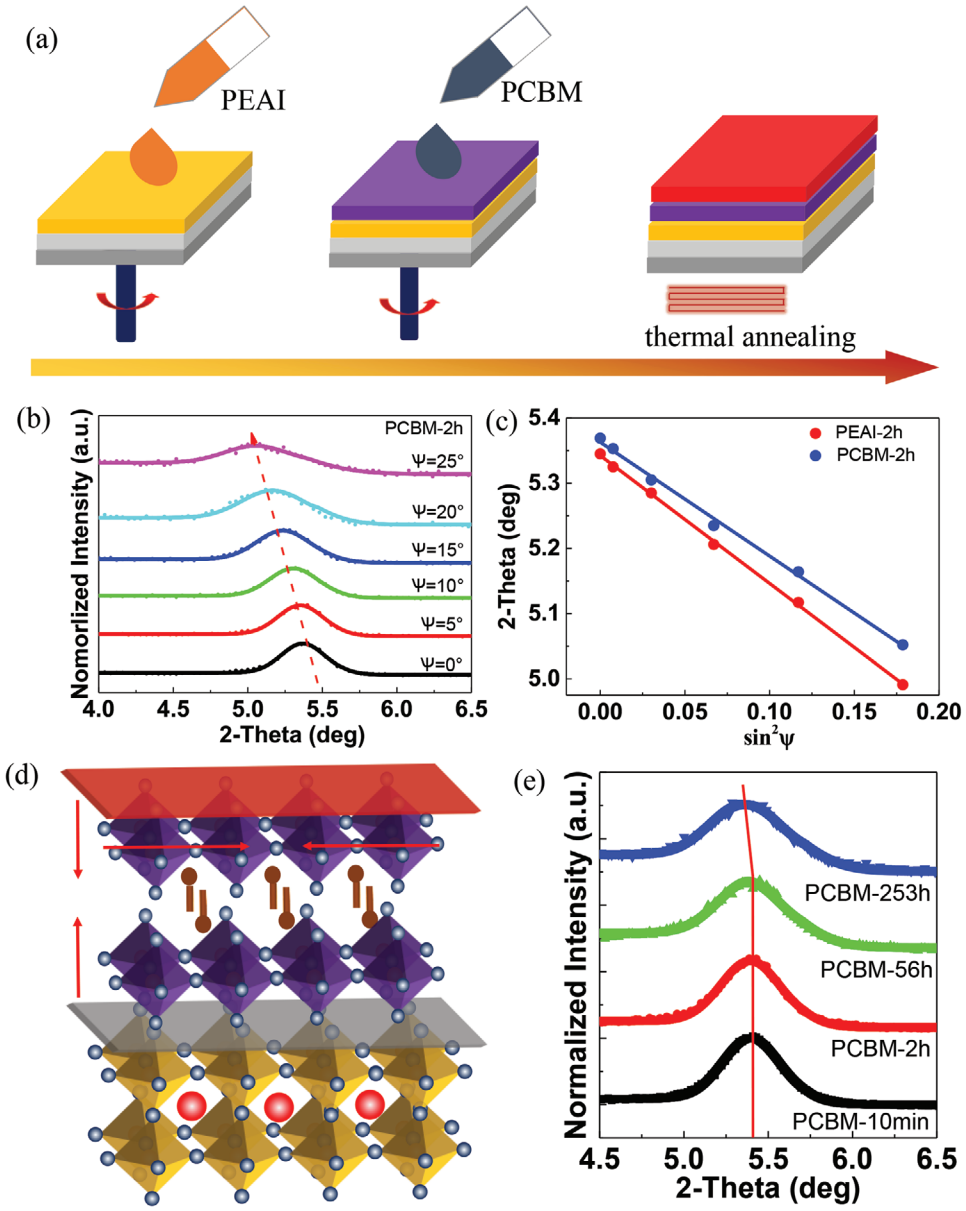

Figure 3. a) Optimized 2D/3D perovskite processing procedures. b) GIXRD spectrums at different tilt angles for the PCBM-2 h thin film. c) Residual tensile stresses of PEA_2PbI_4 under different preparation technology. d) Schematic diagram for stress compensation caused by covering PCBM. e) Magnified diffraction peaks of (002) plane from 2D perovskite prepared by optimized method under varying annealing time.

novel strategy not only compensates stress, but also restrains the lattice expansion while promoting the diffusion passivation. Similar to the PEAI-2 h thin film, the peak intensity of the 2D perovskite for the PCBM-2 h sample decreased to some extent while that of the 3D counterpart maintained stable. The major difference is however that the intensity decays at a much slower rate for the PCBM-2 h sample. When heating the perovskite thin films, PEA_2PbI_4 near the 3D perovskite may react with it and form a mixed 2D–3D structured $(PEA)_2(MA)_{m-1}Pb_mI_{3m+1}$, thereby weakening the diffraction peaks of PEA_2PbI_4. As the presence of PCBM inhibits the ion migration, the above reaction speed is reduced. Therefore, the diffraction peak intensities for the PCBM-2 h sample decay more slowly.

To further verify the diffusion passivation, we have prepared electron-only devices (ITO/SnO_2/perovskite/PCBM/ZnO/Ag) to investigate the defect-state density. The characterization results are shown in **Figure 4**a. The applied voltage at the kink point is generally known as the trap-filled limit voltage (V_{TFL}), which allows to calculate the trap density as follows.[43]

$$N_{trap} = \frac{2\varepsilon\varepsilon_0 V_{TFL}}{ed^2} \quad (2)$$

where d is the thickness of perovskite film (here: 500 nm, see Figure S10, Supporting Information), ε is the relative dielectric constant of perovskite, and ε_0 is the permittivity of vacuum.

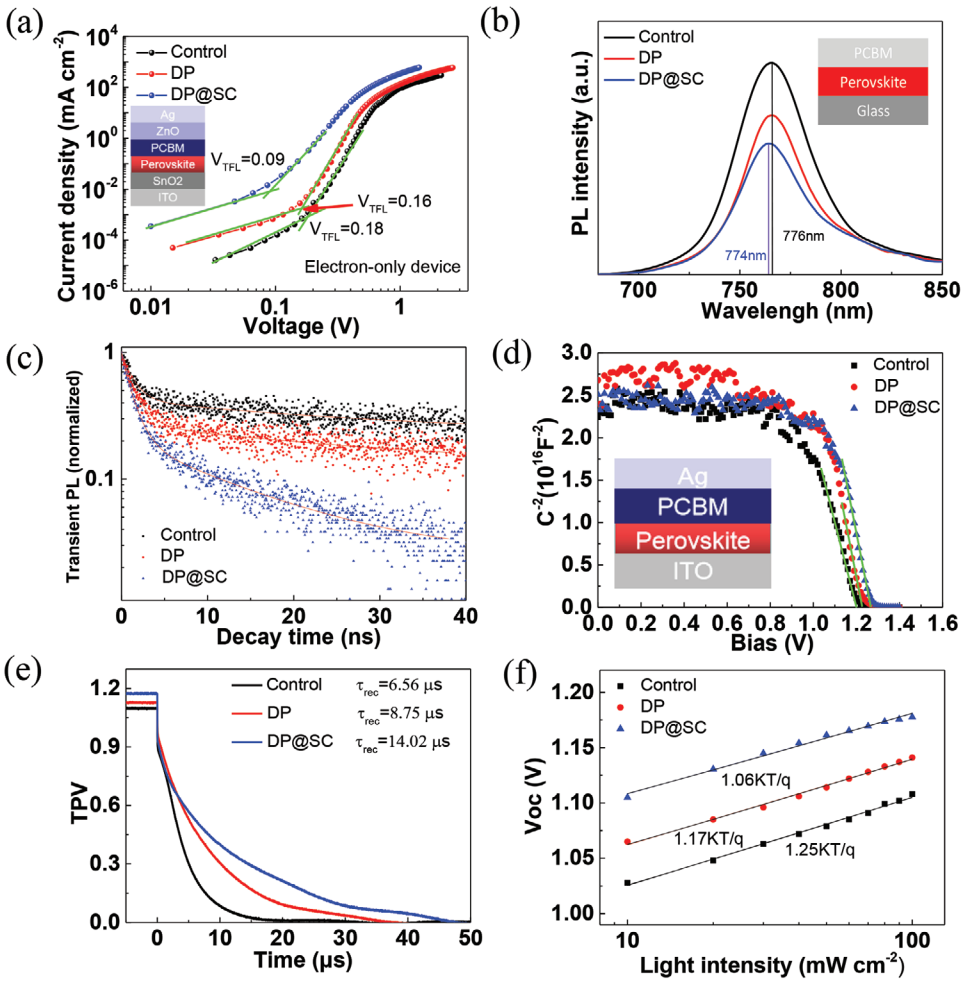

Figure 4. a) Logarithm of *J*–*V* curves in the dark for Control, DP, and DP@SC devices (inset shows the device structure). b) Steady-state PL of perovskite films (inset shows the device structure). c) TRPL of perovskite films. d) Mott–Schottky fitting of capacitance–voltage (C^{-2}–V) plots for Control, DP, and DP@SC devices (inset displays the device structure). e) Carrier recombination lifetime measured by transient photovoltage (TPV). f) V_{OC} dependence as a function of light intensity.

After fitting and calculating, the corresponding electron trap densities are 2.78×10^{15}, 2.47×10^{15}, and 1.39×10^{15} cm^{-3} for three devices, which is consistent with our insight that 2D perovskites diffusion strengthens the passivation effect while strain compensation decreases the formation energy of defects. Because the diffusion passivation (DP) is realized for the PEAI-2 h sample, and diffusion passivation and strain compensation (SC) simultaneously are achieved for the PCBM-2 h sample, they are abbreviated as DP and DP@SC for simplicity, and hereafter the PEAI-10 min is named Control.

It is also noted that the steady-state PL of the perovskite film with a charge transport layer (perovskite films were deposited on glass) has a tendency of show a weakened emission intensity upon prolonged thermal annealing (Figure 4b). It indicates that non-radiative recombination caused by defects at grain boundaries is further suppressed due to diffusion passivation. We also observed that the emission peak for DP@SC thin film has a slight blue shift (from 776 to 774 nm), which is attribute to reduced tensile stress. This was further confirmed by the time resolved photoluminescence (TRPL) spectra (Figure 4c and Table S4, Supporting Information): Shorter PL lifetime implies a lower recombination velocity during carrier transport.[44]

The increased V_{OC} value was confirmed via capacitance–voltage (*C*–*V*) analysis. As shown in Figure 4d, the DP@SC device possesses a much higher V_{bi} of 1.26 V than both the DP (1.23 V) and the Control (1.20 V) devices, which is consistent with the tendency of V_{OC} values for the different types of devices as extracted from the *J*–*V* results. The improvement in V_{bi} represents a larger driving force for photogenerated charge carrier transportation to the electrode.[45,46] Furthermore, the charge recombination time constants (t_{rec}) have been derived from transient voltage measurements performed under open-circuit conditions, as illustrated in Figure 4e. The DP@SC device with a V_{OC} of 1.18 V exhibits a carrier decay time of 14.02 µs, which is almost two times greater than that of the Control (6.56 µs) and DP devices (8.75 µs). These results imply slower charge recombination in the DP@SC device.[47] Figure 4f shows V_{OC} versus light intensity plots, providing additional information on charge recombination in PSCs. The DP device exhibits a slope of 1.17 kT q^{-1}. For DP@SC device, the slope decreases

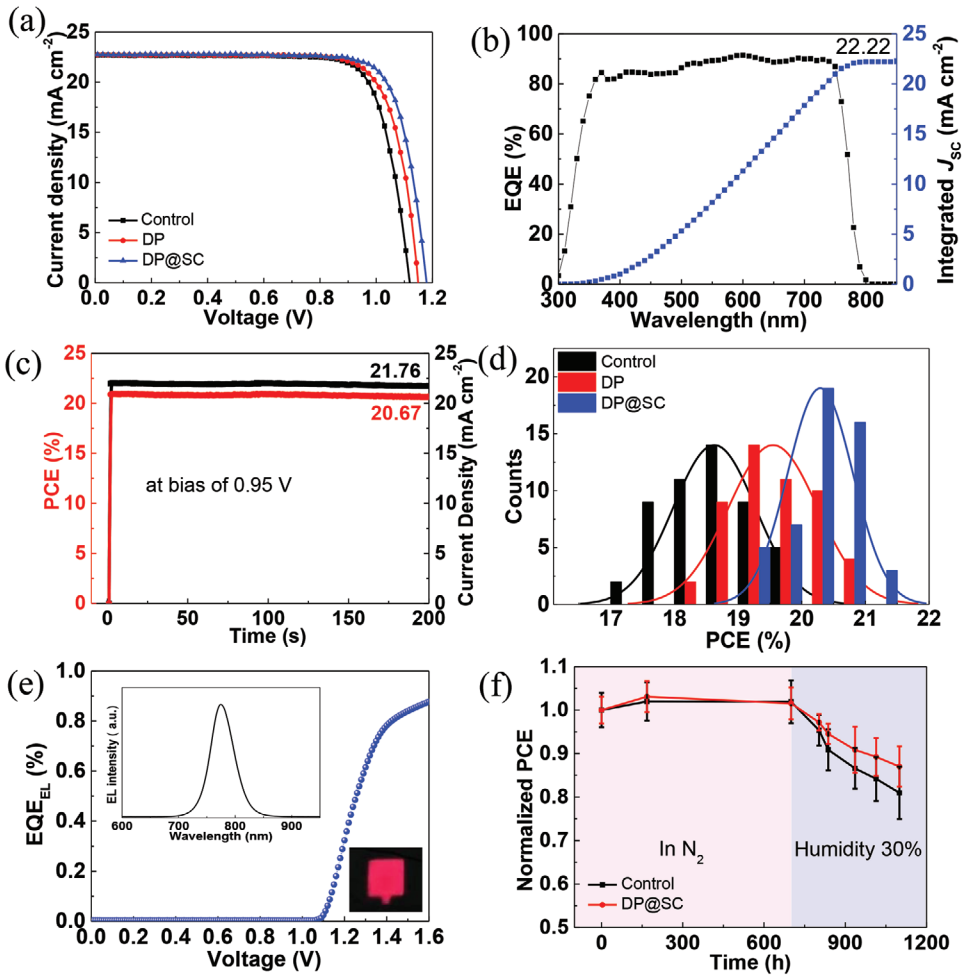

Figure 5. a) The typical *J–V* curves for Control, DP, and DP@SC devices. b) EQE spectrum for DP@SC device. c) Steady-state PCEs for DP@SC device. d) Statistical histogram for PCE of Control, DP, and DP@SC devices, represented for 50 data points. e) EQE of EL as a function of voltage. The left inset shows the corresponding EL spectrum over wavelength. The right inset shows a solar cell with one active area. f) Stability of Control and DP@SC devices in N_2 and air environment (≈30 RH% at room temperature).

to 1.06 kT q^{-1}, which indicates a further suppression of trap-assisted carrier recombination through strain compensation.[48]

The effects of diffusion passivation and strain compensation were examined by preparing corresponding complete devices and measuring their *J–V* characteristics (**Figure 5**a, Figure S11, Supporting Information). Enhanced V_{OC} and FF were observed for DP and DP@SC devices. The DP@SC cell exhibits a J_{SC} of 22.76 mA cm^{-2}, a remarkably high V_{OC} of 1.18 V and a FF of 79.3%, resulting in a noteworthy PCE of 21.31% (the certified efficiency is 20.22%, and the certification document is shown in Figure S12, Supporting Information). Obviously, it shows a considerable leap in PCE from ≈19% to ≈21% upon introduction of the strain-compensation layer compared to the Control device, and a V_{OC} upgrade by 60 mV from 1.12 to 1.18 V. A larger area, square-centimeter (1.0 cm^2) DP@SC PSC has also been fabricated and a high PCE of 18.58% has been obtained (Figure S13, Supporting Information). A summary of earlier reported PCE versus V_{OC} data of organic–inorganic PSCs capped with PEAI is shown in Figure S14 and Table S5, Supporting Information, indicating that our result is the best for p-i-n structured devices. Figure 5b shows the external quantum efficiencies (EQE) spectrum and integrated J_{SC} for our DP@SC device. The integrated J_{SC} of 22.22 mA cm^{-2} agrees well with the measured J_{SC}. The steady photocurrent density and PCE under prolonged forward bias of 0.95 V are plotted as a function of measurement time (Figure 5c). The photocurrent density and stabilized power output (SPO) of the unsealed devices remain stable for 200 s, and a highly stable PCE of 20.67% with J_{SC} of 21.76 mA cm^{-2} is obtained. The SPO value is slightly lower than the efficiency obtained from the *J–V* result, which may be attributed to a tiny hysteresis effect (with hysteresis index of 0.037). Figure 5d shows the PCE distribution histogram for the three classes of devices; the corresponding photovoltaic metrics are summarized in Figure S15, Supporting Information. It should be noted that the DP@SC devices exhibit excellent repeatability with a very small standard deviation (±0.51), in contrast to DP (±0.55) and Control (±0.65) devices, indicating that the compensation of tensile strain and the diffusion passivation improves the reproducibility of cell performance.

To prove the universality of the optimization strategy, we also introduced other 2D perovskites, for example, BA_2PbI_4, NMA_2PbI_4 (NMA: 1-naphthylmethylamine), and PMA_2PbI_4 (PMA: phenylmethanamine), of which BA_2PbI_4 has been verified to possess weak interlayer molecular interaction,[27] on 3D perovskite films, and fabricated corresponding solar cells. As a result, all three types of PSCs exhibited improvement in photovoltaic performance (see Figure S16, Supporting Information).

It has been reported that electroluminescent quantum efficiency (EQE_{EL}) of solar cells in the dark operating as a light-emitting diode (LED) under bias voltage can be used to analyze the limiting V_{OC} of recombination mechanisms in the devices.[49,50] A higher emission efficiency through radiative recombination is accompanied by a higher V_{OC} based on following expression,

$$V_{OC} = \frac{K_B T}{q} \ln\left(\mathrm{EQE}_{EL}\frac{J_{ph}}{J_{em,0}} + 1\right) \quad (3)$$

where K_B is Boltzmann's constant, T is the temperature, and $J_{em,0}$ is the current due to re-emitted photons. Note that the EQE_{EL} value used for this calculation is taken at an injection current in the dark that is equal to the photocurrent of the device under illumination.

The EQE_{EL}–V characteristics of the best-performing DP@SC device show an approximate EQE_{EL} of 0.5% at 1.25 V for a driving current density of 22.2 mA cm^{-2} (Figure 5e) and thus a low non-radiative V_{OC} loss of 140 mV is deduced, which is attributed to the low defect density. The EL emission spectrum (emission peak is located at 775 nm) and an image of the device are inserted in Figure 5e. This non-radiative V_{OC} loss of 140 mV implies a calculated V_{OC} value of 1.18 V (V_{OC} = 1.32 V − 0.14 V = 1.18 V, where 1.32 V is the theoretical radiative limit V_{OC} of solar cell with calibrated bandgap of 1.60 eV as shown in Figure S17, Supporting Information), which is consistent with the measured value. Here, the calculation of the theoretical radiative limit is according to the method described by Steve Byrnes.[51] The corresponding EQE_{EL}–J characteristics is displayed in Figure S18, Supporting Information.

The effect of trap-assisted recombination on the device performance is more pronounced under weak light conditions.[52] The PCE of DP@SC device have been measured at different illumination intensities (Figure S19 and Table S6, Supporting Information). The DP@SC cell has a PCE of 22.09% with J_{SC} of 18.82 mA cm^{-2}, V_{OC} of 1.14 V, FF of 0.82 under 0.8-sun illumination. The relationship between normalized FF and light intensity is also plotted (Figure S19, Supporting Information). It can be observed that the FF value of DP@SC device has a slight upward trend as the light intensity weakens, which denotes an effective reduction of trap-assisted recombination due to the diffusion passivation and strain compensation.

In addition, the stability of the Control and the DP@SC devices has also been analyzed. The samples were initially placed in a N_2 glovebox for 700 h and then in ambient air atmosphere (≈30 RH%) for 400 h, as shown in Figure 5f. It can be seen that the stability of the two devices is almost the same in the N_2 environment, but the DP@SC device shows better stability in ambient air environment. This is attributed to the protective function of the PEA_2PbI_4 layer with low tensile stress, namely, it shields the surface and grain boundary of the perovskite from moisture from the air and inhibits ion migration.[53,54]

In summary, a highly stable 2D/3D heterostructure was achieved by using a PCBM layer as a stress-compensation layer. PCBM counteracts the lattice expansion generated by the migration of MA^+ and I^- ions, while compensating the tensile stress of the 2D perovskite underneath. In addition, a diffusion passivation mechanism of the 2D perovskite, induced by thermal annealing, was confirmed. The synergistic effect of strain-compensation and diffusion passivation results in the suppression of ion migration and of non-radiative recombination. PEAI-based 2D/3D heterostructure perovskite devices with a p-i-n structure achieved an unprecedented certified PCE of 20.22%, and showed robustness and high repeatability. The innovation described here provides a new paradigm enabling a reliable implementation of 2D materials in photovoltaic applications.

Experimental Section

Materials and Methods: Lead iodide (PbI_2, 99.9985%) and cesium iodide (CsI, 99.999%) were purchased from Alfa Aesar. Poly[bis(4-phenyl)(2,4,6-trimethylphenyl) amine (PTAA, M_n = 6000–15 000), formamidinium iodide (FAI, ≥99.5%), methylammonium bromide (MABr, ≥99.5%), and phenethylammonium iodide (PEAI, ≥99.5%) were purchased from Xi'an polymer Light Technology Corp. PCBM was purchased from Lumtec. Lead bromide ($PbBr_2$, 99.999%), dimethyl sulfoxide (DMSO, ≥99.9%), *N*,*N*-dimethylformamide (DMF, 99.8%), and chlorobenzene (99.8%) were obtained from Sigma-Aldrich. Isopropanol (≥99.9%) and ethyl acetate (99%) were purchased from Aladdin. ZnO nanoparticle solution (2.5 wt% ZnO in isopropanol, particle size: 12 nm) was received from Avantama.

Fabrication of Solar Cell: ITO-coated glass (OPV Tech Co., Ltd.) substrate with sheet resistance of 17 Ω sq^{-1} was sequentially washed by ultrasonication with deionized water, ethanol, isopropanol, and acetone for 10 min and then treated with oxygen plasma for 10 min. Then, a hole transport layer of PTAA was deposited on ITO substrate by using spin-coating method with precursor of 1.5 mg of PTAA in chlorobenzene (1 mL) at 6000 rpm for 30 s, followed by sintering at 100 °C for 15 min. The above processes were performed in the ambient environment. After that, the perovskite layer was deposited by using one-step spin-coating method in the dry air filled glovebox. The perovskite precursor solution was comprised of $FAPbI_3$ (260 µL), $MAPbBr_3$ (40 µL), and CsI (15 µL). In particular, $FAPbI_3$ precursor solution was prepared by mixing FAI (1.38 M) and PbI_2 (1.5 M) in DMF:DMSO (8:2, v:v). At the same time, $MAPbBr_3$ precursor solution was prepared by mixing MABr (1.38 M) and $PbBr_2$ (1.5 M) in DMF:DMSO (8:2, v:v). Moreover, the stock solution of CsI was prepared by dissolving 390 mg CsI in 1 mL DMSO. The perovskite solution was spin coated with two-step program at 1000 and 4000 rpm for 4 and 30 s, respectively. During the second step, 300 µL of ethylacetate was dropped on spinning substrate for 10 s which prior to end of the program. Then, the substrates were annealed at 100 °C for 20 min. For the original formation of 2D perovskite as a capping layer, the PEAI solution was spin coated on the surface of perovskite layer and then annealed at 100 °C for different time. After that, the PCBM (15 mg mL^{-1} in chlorobenzene) solution was spin coated on perovskite layer at 2000 rpm for 30 s. For the optimized process, 2D perovskite was formed by thermal annealing PEAI-based films at 100 °C after spin coating of PCBM. Furthermore, the ZnO nanoparticles as solution were diluted in IPA (1:1 by volume) and then spin coated onto the PCBM thin film at 2000 rpm for 30 s and annealed at 100 °C for 5 min. Finally, the Ag electrode (120 nm) was evaporated on ZnO layer by using thermal evaporation method and the fixed active area of this electrode was 0.09 cm^2. Note that all the solutions were filtered with 0.22 µm PVDF filters before spin coating.

Characterizations: The crystal structure was characterized by Bruker D8 Advance X-ray diffractometer (XRD) with Cu Kα radiation at 40 kV

and 40 mA. GIXRD patterns were recorded on smartlab XRD. For the HRTEM measurements, cross-sectional lamellae were prepared from the devices using the conventional FIB lift-out technique on a FEI Scios. To reduce FIB-induced damage, a final thinning in the FIB at 2 kV using a beam current of 23 pA was employed. To minimize exposure to air, the data were acquired just after the FIB preparation. HRTEM imaging was performed on a JEOL JEM-3200FS transmission electron microscope in scanning mode at an accelerating voltage of 200 kV. The cross-sectional morphologies of films were analyzed by using scanning electron microscopy (SEM; FEI ApreoLoVac) in which the SEM images were obtained directly from as-prepared films. The transient photovoltage decay curves and dark (current–voltage) *C–V* curves were collected from electrochemical workstation (ZAHNER GIMPS, Germany). The *C–V* curves were obtained by using a digital source meter (Keithley 2400) and a Newport solar simulator (ORIEL-SOI3A) with AM 1.5 G spectrums. The light intensity on the sample was adjusted to 1000 W m^{-2} using a standard Si cell (91150V). A black mask with an aperture area of 9 mm^2 was placed on top of the device to control the illuminated area. The EQE of PSCs were measured by using spectrum corresponding system (Enlitech QE-R), with Si solar cell as a reference to determine the spectral responses. The PL and TRPL spectra were recorded by using a FV1200 laser scanning confocal microscopy in which a 532 nm of pulsed diode laser was used for excitation with repetition rate of 40 MHz and the emission was filtered through 50/50 dichroic beam splitter as well as 700–800 nm long pass filter. The EL spectrum and ERE of the perovskite LED were recorded simultaneously by a commercialized system (XPQY-EQE-350-1100, Guangzhou Xi Pu Optoelectronics Technology Co., Ltd.) that is equipped with an integrated sphere (GPS-4P-SL, Labsphere) and a photodetector array (S7031-1006, Hamamatsu Photonics).

First-Principles Calculations: The first-principles calculations have been performed within the framework of DFT by means of plane wave pseudopotential as implemented in the Vienna Ab initio Simulation Package.[55,56] The electron–ion interactions were described by the projected augmented wave pseudopotentials[57] with the 1s (H), 2s and 2p (C), 2s and 2p (N), 5s and 5p (I) and 5d, 6s and 6p (Pb) electrons treated explicitly as valence electrons. The generalized gradient approximation formulated by Perdew, Burke, and Ernzerhof[58] was used as the exchange correlation functional. We used a kinetic energy cutoff of 400 eV for wavefunction expansion and a $2 \times 2 \times 1$ Monkhorst–Pack k-point mesh for electronic Brillouin zone integration of 2D Ruddlesden–Popper hybrid halide perovskites. The structures under the biaxial stretch conditions were optimized by fixing modified *a* and *b* axes and only relaxing *c* axis, and the total energy minimization was converged to below $1 \times E^{-5}$ eV $Å^{-1}$. To properly consider the long-range Van der Waals interaction, which is non-negligible for hybrid perovskites involving organic molecules, the Van der Waals optB86b functional was adopted.

Supporting Information

Supporting Information is available from the Wiley Online Library or from the author.

Acknowledgements

C.Z. and S.W. contributed equally to this work. This work was supported by the National Key Research and Development Program of China (Grant No. 2018YFB1500103), the Fundamental Research Funds for the Central Universities (11619103), and Scientific Research Fund of Natural Science Foundation of Guangdong University of Petrochemical Technology (No. 2019rc019).

Conflict of Interest

The authors declare no conflict of interest.

Keywords

2D/3D perovskites, diffusion passivation, lattice expansion, perovskite solar cells, strain compensation

Received: June 20, 2020
Revised: August 30, 2020
Published online: October 2, 2020

[1] W. S. Yang, J. H. Noh, N. J. Jeon, Y. C. Kim, S. Ryu, J. Seo, S. I. Seok, *Science* **2015**, *348*, 1234.
[2] W. S. Yang, B.-W. Park, E. H. Jung, N. J. Jeon, Y. C. Kim, D. U. Lee, S. S. Shin, J. Seo, E. K. Kim, J. H. Noh, *Science* **2017**, *356*, 1376.
[3] Q. Jiang, Y. Zhao, X. Zhang, X. Yang, Y. Chen, Z. Chu, Q. Ye, X. Li, Z. Yin, J. You, *Nat. Photonics* **2019**, *13*, 460.
[4] Z. Liu, L. Krückemeier, B. Krogmeier, B. Klingebiel, J. A. Márquez, S. Levcenko, S. Öz, S. Mathur, U. Rau, T. Unold, *ACS Energy Lett.* **2018**, *4*, 110.
[5] J. Peng, J. I. Khan, W. Liu, E. Ugur, T. Duong, Y. Wu, H. Shen, K. Wang, H. Dang, E. Aydin, *Adv. Energy Mater.* **2018**, *8*, 1801208.
[6] D. Luo, R. Su, W. Zhang, Q. Gong, R. Zhu, *Nat. Rev. Mater.* **2020**, *5*, 44.
[7] C. Liu, Y. Yang, C. Zhang, S. Wu, L. Wei, F. Guo, G. M. Arumugam, J. Hu, X. Liu, J. Lin, R. E. I. Schropp, Y. Mai, *Adv. Mater.* **2020**, *32*, e1907361.
[8] D. Bi, W. Tress, M. I. Dar, P. Gao, J. Luo, C. Renevier, K. Schenk, A. Abate, F. Giordano, J.-P. C. Baena, *Sci. Adv.* **2016**, *2*, e1501170.
[9] H. Zhang, Y. Wu, C. Shen, E. Li, C. Yan, W. Zhang, H. Tian, L. Han, W. H. Zhu, *Adv. Energy Mater.* **2019**, *9*, 1803573.
[10] M. A. Mahmud, T. Duong, Y. Yin, H. T. Pham, D. Walter, J. Peng, Y. Wu, L. Li, H. Shen, N. Wu, N. Mozaffari, G. Andersson, K. R. Catchpole, K. J. Weber, T. P. White, *Adv. Funct. Mater.* **2020**, *30*, 1907962.
[11] M. Saliba, T. Matsui, K. Domanski, J.-Y. Seo, J.-P. Correa-Baena, M. K. Nazeeruddin, S. M. Zakeeruddin, W. Tress, A. Abate, A. Hagfeldt, M. Grätzel, *Energy Environ. Sci.* **2016**, *9*, 1989.
[12] Z. Ni, C. Bao, Y. Liu, Q. Jiang, W.-Q. Wu, S. Chen, X. Dai, B. Chen, B. Hartweg, Z. Yu, *Science* **2020**, *367*, 1352.
[13] Z. Wang, Q. Lin, F. P. Chmiel, N. Sakai, L. M. Herz, H. J. Snaith, *Nat. Energy* **2017**, *2*, 17135.
[14] D. S. Lee, J. S. Yun, J. Kim, A. M. Soufiani, S. Chen, Y. Cho, X. Deng, J. Seidel, S. Lim, S. Huang, *ACS Energy Lett.* **2018**, *3*, 647.
[15] C. C. Zhang, S. Yuan, Y. H. Lou, Q. W. Liu, M. Li, H. Okada, Z. K. Wang, *Adv. Mater.* **2020**, *32*, 2001479.
[16] Y. Zhao, J. Duan, Y. Wang, X. Yang, Q. Tang, *Nano Energy* **2020**, *67*, 104286.
[17] H. Wang, C. Zhu, L. Liu, S. Ma, P. Liu, J. Wu, C. Shi, Q. Du, Y. Hao, S. Xiang, *Adv. Mater.* **2019**, *31*, 1904408.
[18] H. B. Vailionis, Z. Liao, J. Smit, G. Rijnders, M. Huijben, G. Koster, *Appl. Phys. Lett.* **2014**, *105*, 131906.
[19] J. Hu, C. Wang, S. Qiu, Y. Zhao, E. Gu, L. Zeng, Y. Yang, C. Li, X. Liu, K. Forberich, *Adv. Energy Mater.* **2020**, *10*, 2000173.
[20] J. Tong, Z. Song, D. H. Kim, X. Chen, C. Chen, A. F. Palmstrom, P. F. Ndione, M. O. Reese, S. P. Dunfield, O. G. Reid, *Science* **2019**, *364*, 475.
[21] Y. Zhang, Y. Liu, Z. Yang, S. F. Liu, *J. Energy Chem.* **2018**, *27*, 722.
[22] L. Xiong, Y. Guo, J. Wen, H. Liu, G. Yang, P. Qin, G. Fang, *Adv. Funct. Mater.* **2018**, *28*, 1802757.
[23] E. Mosconi, E. Ronca, F. De Angelis, *J. Phys. Chem. Lett.* **2014**, *5*, 2619.
[24] H.-S. Yoo, N.-G. Park, *Sol. Energy Mater. Sol. Cells* **2018**, *179*, 57.
[25] Y. Hu, J. Schlipf, M. Wussler, M. L. Petrus, W. Jaegermann, T. Bein, P. Müller-Buschbaum, P. Docampo, *ACS Nano* **2016**, *10*, 5999.

[26] H. Tsai, R. Asadpour, J.-C. Blancon, C. C. Stoumpos, O. Durand, J. W. Strzalka, B. Chen, R. Verduzco, P. M. Ajayan, S. Tretiak, *Science* **2018**, *360*, 67.
[27] D.-J. Xue, Y. Hou, S.-C. Liu, M. Wei, B. Chen, Z. Huang, Z. Li, B. Sun, A. H. Proppe, Y. Dong, M. I. Saidaminov, S. O. Kelley, J. S. Hu, E. H. Sargent, *Nat. Commun.* **2020**, *11*, 1514.
[28] C. Zhu, X. Niu, Y. Fu, N. Li, C. Hu, Y. Chen, X. He, G. Na, P. Liu, H. Zai, Y. Ge, Y. Lu, X. Ke, Y. Bai, S. Yang, P. Chen, Y. Li, M. Sui, L. Zhang, H. Zhou, Q. Chen, *Nat. Commun.* **2019**, *10*, 815.
[29] D. Kim, J. S. Yun, P. Sharma, D. S. Lee, J. Kim, A. M. Soufiani, S. Huang, M. A. Green, A. W. Ho-Baillie, J. Seidel, *Nat. Commun.* **2019**, *10*, 444.
[30] K.-z. Du, Q. Tu, X. Zhang, Q. Han, J. Liu, S. Zauscher, D. B. Mitzi, *Inorg. Chem.* **2017**, *56*, 9291.
[31] J. Zhao, Y. Deng, H. Wei, X. Zheng, Z. Yu, Y. Shao, J. E. Shield, J. Huang, *Sci. Adv.* **2017**, *3*, eaao5616.
[32] J. Li, Q. Dong, N. Li, L. Wang, *Adv. Energy Mater.* **2017**, *7*, 1602922.
[33] H. Ren, S. Yu, L. Chao, Y. Xia, Y. Sun, S. Zuo, F. Li, T. Niu, Y. Yang, H. Ju, *Nat. Photonics* **2020**, *14*, 154.
[34] J. Even, L. Pedesseau, C. Katan, *ChemPhysChem* **2014**, *15*, 3733.
[35] C. Ma, D. Shen, T. W. Ng, M. F. Lo, C. S. Lee, *Adv. Mater.* **2018**, *30*, 1800710.
[36] Y. Shao, Y. Fang, T. Li, Q. Wang, Q. Dong, Y. Deng, Y. Yuan, H. Wei, M. Wang, A. Gruverman, *Energy Environ. Sci.* **2016**, *9*, 1752.
[37] C. Eames, J. M. Frost, P. R. Barnes, B. C. O'Regan, A. Walsh, M. S. Islam, *Nat. Commun.* **2015**, *6*, 7497.
[38] C. Fei, H. Wang, *Org. Electron.* **2019**, *68*, 143.
[39] C. Bi, Y. Shao, Y. Yuan, Z. Xiao, C. Wang, Y. Gao, J. Huang, *J. Mater. Chem. A* **2014**, *2*, 18508.
[40] Z. Cheng, J. Lin, *CrystEngComm* **2010**, *12*, 2646.
[41] G. Paterno, A. J. Warren, J. Spencer, G. Evans, V. G. A. Sakai, J. Blumberger, F. Cacialli, *J. Mater. Chem. C* **2013**, *1*, 5619.
[42] J. Xu, A. Buin, A. H. Ip, W. Li, O. Voznyy, R. Comin, M. Yuan, S. Jeon, Z. Ning, J. J. McDowell, P. Kanjanaboos, J. P. Sun, X. Lan, L. N. Quan, D. H. Kim, I. G. Hill, P. Maksymovych, E. H. Sargent, *Nat. Commun.* **2015**, *6*, 7081.
[43] W. Li, C. Zhang, Y. Ma, C. Liu, J. Fan, Y. Mai, R. E. Schropp, *Energy Environ. Sci.* **2018**, *11*, 286.
[44] C. Liu, W. Li, C. Zhang, Y. Ma, J. Fan, Y. Mai, *J. Am. Chem. Soc.* **2018**, *140*, 3825.
[45] J. Ma, Z. Lin, X. Guo, L. Zhou, J. Su, C. Zhang, Z. Yang, J. Chang, S. Liu, Y. Hao, *Sol. RRL* **2019**, *3*, 1900096.
[46] L. Zhou, Z. Lin, Z. Ning, T. Li, X. Guo, J. Ma, J. Su, C. Zhang, J. Zhang, S. Liu, *Sol. RRL* **2019**, *3*, 1900293.
[47] E. Bi, H. Chen, F. Xie, Y. Wu, W. Chen, Y. Su, A. Islam, M. Grätzel, X. Yang, L. Han, *Nat. Commun.* **2017**, *8*, 15330.
[48] T. Singh, T. Miyasaka, *Adv. Energy Mater.* **2018**, *8*, 1700677.
[49] U. Rau, *Phys. Rev. B* **2007**, *76*, 085303.
[50] T. Kirchartz, U. Rau, *Phys. Status Solidi A* **2008**, *205*, 2737.
[51] W. Shockley, H. J. Queisser, *J. Appl. Phys.* **1961**, *32*, 510.
[52] W.-Q. Wu, Z. Yang, P. N. Rudd, Y. Shao, X. Dai, H. Wei, J. Zhao, Y. Fang, Q. Wang, Y. Liu, *Sci. Adv.* **2019**, *5*, eaav8925.
[53] C. Smith, E. T. Hoke, D. Solis-Ibarra, M. D. McGehee, H. I. Karunadasa, *Angew. Chem., Int. Ed.* **2014**, *53*, 11232.
[54] N. Li, Z. Zhu, Q. Dong, J. Li, Z. Yang, C. C. Chueh, A. K. Y. Jen, L. Wang, *Adv. Mater. Interfaces* **2017**, *4*, 1700598.
[55] G. Kresse, J. Furthmüller, *Comput. Mater. Sci.* **1996**, *6*, 15.
[56] G. Kresse, J. Furthmüller, *Phys. Rev. B* **1996**, *54*, 11169.
[57] J. P. Perdew, K. Burke, M. Ernzerhof, *Phys. Rev. B* **1994**, *50*, 17953.
[58] J. P. Perdew, K. Burke, M. Ernzerhof, *Phys. Rev. Lett.* **1996**, *77*, 3865.